Terahertz Power Divider Using Symmetric CPS Transmission Line on a Thin Membrane

WALID GOMAA [ID]1, ROBERT LEVI SMITH1, (Member, IEEE), HADI ESMAEILSABZALI2, AND THOMAS E. DARCIE1, (Fellow, IEEE)

[1]Department of Electrical and Computer Engineering, University of Victoria, Victoria, BC V8P 5C2, Canada
[2]4D LABS, Simon Fraser University, Burnaby, BC V5A 1S6, Canada

Corresponding author: Walid Gomaa (walidgomaa@uvic.ca)

ABSTRACT Recently, research has focused on developing efficient wave-guided THz system-on-chip (TSoC) components to reduce physical bulk, loss and cost of free-space THz systems. We recently demonstrated a TSoC platform using a coplanar-stripline (CPS) transmission-line on a 1 μm-thin membrane to generate and detect THz-bandwidth pulses with low loss and low dispersion up to 1.5 THz. In this paper, we demonstrate experimentally an in-phase THz power divider (TPD) at frequency 0.65 THz using the CPS transmission line defined by photolithography on a thin membrane. Measured pulses show close agreement with simulation results. The spectral power density of the measured THz-bandwidth pulses at the output ports are identical at the frequency of 0.65 THz with less than 1 dB power imbalance over a wide spectrum up to 1 THz.

INDEX TERMS Terahertz waveguide, coplanar stripline, power divider, thin membrane.

I. INTRODUCTION

Recently, we demonstrated a THz system-on-chip (TSoC) platform using a 1 μm-thin Si_3N_4 membrane in which thin photoconductive switches (PCSs) were bonded directly on a coplanar-stripline (CPS) transmission-line to generate and detect THz-bandwidth pulses with low loss and low dispersion [1]. Using that approach, it becomes possible to develop different active and passive TSoC components, such as power dividers (PDs), which are essential passive components for future TSoCs.

Power dividers have been proposed with numerous configurations in microwave spectrum, such as T-junction, Y-junction and Wilkinson. These power dividers were implemented using waveguides [2]–[4], microstrip [5]–[9], coplanar waveguide (CPW) [10]–[13], substrate integrated waveguide (SIW) [14]–[18], complementary split-ring resonators (CSRRs) [19], and many research results that are based on two types of waveguide and transmission line such as microstrip-slotline [20]–[25], microstrip-CPS [26], [27] CPW-microstrip [28], CPW-asymmetric coplanar stripline (ACPS) [29]–[32], and slotline-ACPS [33], [34].

Furthermore, many mm-wave/THz PDs have been introduced using different structures such as waveguide [35]–[37], Wilkinson [38], [39], planar Goubau lines (PGLS) [40], graphene plasmonic waveguide [41], electromagnetic bandgap (EBG) waveguide [42], directional coupler waveguide [43], substrate integrated coaxial line [44], and CPW-CPS [45].

In this paper, we used the membrane platform introduced in [1] to demonstrate experimentally a 3-dB in-phase THz power divider (TPD) with a design frequency of 0.65 THz using a symmetric CPS transmission line on a 1 μm-thin Si_3N_4 membrane.

Prior work using planar transmission lines (i.e. microstrip, slotline, CPW, CPS) was targeted mainly at microwave frequencies and implemented by integrating two types of transmission lines (i.e. one for excitation and the other for the division). Table 1 provides a comparison between the presented work and the prior power dividers demonstrated with the CPS and ACPS transmission lines. The main advantages of using the membrane platform introduced in [1] are bandwidth (up to at least 1.5 THz), fabrication precision, compatibility with conventional photolithographic fabrication, low loss, and low pulse dispersion. The balanced CPS transmission line is desirable for many TSoC designs [46]–[48]. Moreover, the CPS transmission line is

The associate editor coordinating the review of this manuscript and approving it for publication was Dušan Grujić [ID].

TABLE 1. Comparison between the presented work and the prior power dividers demonstrated with CPS and ACPS transmission lines.

Reference	Transmission line	Substrate	Bandwidth (GHz)	Properties (dB)	Notes
[26] - M. Leib et al	Microstrip-CPS	RO4003 $\varepsilon_r = 3.38$ t = 810 μm	3.1 to 12.3	RL =15 IL = 4.6	In-phase
			1 to 12.3	RL =10 IL = 4.6	180° out-of-phase
[27] - P. Wu et al		RT/Duroid 5880 $\varepsilon_r = 2.2$ t = 254 μm	26.5 to 40	RL=10 Isolation = 14.4	In-phase
[29] - L. Fan et al	CPW-ACPS	RT/Duriod 6010 $\varepsilon_r = 10.8$ t = 1524 μm	2 to 4	RL = 21.5 IL = 3.5 Isolation = 24	In-phase
[30] - T. Laneve et al		Si t = 400 μm	21.5 to 23	RL = 22 IL = 0.7	Wilkinson
[31] - M. Scardelletti et al		Si and alumina t = 400 + 500 μm	7.5 to 12.5	RL = 30 IL = 3.55 Isolation = 15	Wilkinson
[32] - K. Hettak et al		Alumina t = 254 μm	19 to 25.5	RL = 30 IL = 3.5 Isolation = 30	Wilkinson
[33] - L. Fan et al	Slotline-ACPS	RT/Duriod 6010 $\varepsilon_r = 10.8$ t = 1524 μm	2.5 to 3.5	RL = 23 IL = 3.8 Isolation = 20.5	180° out-of-phase
[34] - K. W. Wong et al		RT/Duriod 6010 $\varepsilon_r = 10.8$ t = 1270 μm	0.4 to 1.1	RL = 20 IL = 3.3 Isolation = 20	In-phase
[45] - C. Li et al	CPW-CPS	GaAs t = 620 μm	44 to 112	RL = 18 IL = 4.3 Isolation = 20	In-phase
Presented work	CPS	Si3N4 membrane t = 1 μm	630 to 670	RL = 40 IL = 3.1 Isolation = 30	In-phase & 180° out-of-phase

RL = return loss and IL = insertion loss.

appropriate for designing and combining different TSoC components (such as power dividers, couplers, filters, chokes, stubs, etc.) either in series or parallel configurations. To the best of our knowledge, this is the first THz power divider that uses CPS transmission line in the entire structure. Table 1 illustrates that this work is unique both in terms of high frequencies of operation and the use of a thin membrane substrate.

II. THEORY

Considering the lossless power divider shown in Fig. 1, we model the CPS transmission lines as a port with impedances Z_1 for input and two series-connected output ports Z_2 and Z_3.

To match all ports, the impedance of the input port (Z_1) must be matched to the load impedance Z_L (i.e. the reflection coefficient $\Gamma = 0$ for $Z_1 = Z_L$). A quarter-wave impedance transformer, Z_m, is required to match the output ports with the input port. The impedance of input port Z_1 is related to the equivalent impedances of each output ports (i.e. Z_{2i} represents the series equivalent of Z_m and Z_2, while Z_{3i} represents the
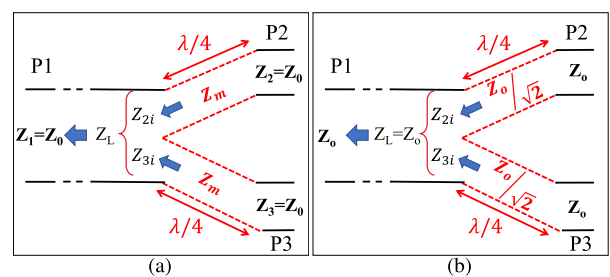

FIGURE 1. Schematic diagram of THz power dividers.

series equivalent of Z_m and Z_3):

$$Z_1 = Z_{2i} + Z_{3i} \quad (1)$$

The power division ratio α, which is the ratio of the power delivered to the output ports, P_2 and P_3 respectively, is related to the input impedance of the output ports Z_{2i} and Z_{3i}:

$$\alpha = \frac{P_3}{P_2} = \frac{Z_{3i}}{Z_{2i}} \quad (2)$$

After rearranging equations (1) and (2), the equivalent input impedance of the two output ports (Z_{2i} and Z_{3i})
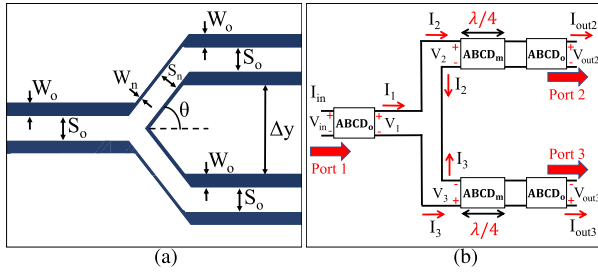
FIGURE 2. (a) Structure of TPD using CPS transmission line on a thin membrane. (b) ABCD matrix representation of the TPD.

FIGURE 3. The transmission and reflection coefficients of the TPD using the ABCD representation.

are:

$$Z_{2i} = Z_1/(1 + \alpha) \tag{3a}$$

$$Z_{3i} = Z_1/(1 + 1/\alpha) \tag{3b}$$

For equal power division ratio $\alpha = 1$ (i.e. $P_2 = P_3 = P_1/2$) and identical CPS transmission line impedance at input and output ports ($Z_1 = Z_2 = Z_3 = Z_0$), the equivalent input impedance of the two output ports will be: $Z_{2i} = Z_{3i} = Z_0/2$. Therefore, the $\lambda/4$ impedance transformer must have Z_m given by:

$$Z_m = \sqrt{Z_2.Z_{2i}} = \sqrt{Z_0 . Z_0/2} = Z_0/\sqrt{2} \tag{4}$$

Figure 2(a) illustrates the structure of TPD using symmetric CPS transmission lines on a 1 μm-thin membrane. The input and output ports have a CPS geometry, stripline width W_0 and separation S_0, and impedance Z_0. The $\lambda/4$ impedance transformer was represented by a CPS transmission line with stripline width W_n, separation S_n and impedance $Z_0/\sqrt{2}$.

Since the output ports are connected in series (1) we can use the ABCD transmission matrix method to model the CPS-PD. Figure 2(b) illustrates the ABCD representation of the TPD using CPS transmission line. The circuit from the input port to one of the output ports is modelled by four cascaded ABCD matrices [49]. The matched input and output ports are represented by $ABCD_0$, and the $\lambda/4$ impedance transformers are represented by $ABCD_m$. For the series-connected ports, the voltages and currents relations are given by $V_1 = 2V_2 = -2V_3$ and $I_1 = I_2 = -I_3$ (see Fig.2(b)) which in matrix form is given by:

$$\begin{bmatrix} V_1 \\ I_1 \end{bmatrix} = ABCD_s \cdot \begin{bmatrix} V_2 \\ I_2 \end{bmatrix} = \begin{bmatrix} 2 & 0 \\ 0 & 1 \end{bmatrix} \begin{bmatrix} V_2 \\ I_2 \end{bmatrix}$$

$$= -\begin{bmatrix} 2 & 0 \\ 0 & 1 \end{bmatrix} \begin{bmatrix} V_3 \\ I_3 \end{bmatrix}. \tag{5}$$

The $ABCD_s$ matrix assumes an equal power distribution ($P_2 = P_3 = P_1/2$) which can be verified by calculating $P_2/P_1 = (1/2\ Re\{V_2 I_2^*\})/(1/2\ Re\{V_1 I_1^*\})$. Note that $ABCD_s$ is positive and negative for Port 2 and Port 3, respectively. The total ABCD matrix that relates the output port, P_2, with the
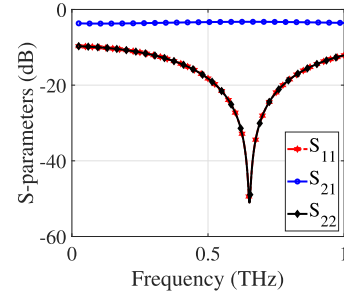
input port, P_1, is given by:

$$ABCD_t = ABCD_0 \times ABCD_s \times ABCD_m \times ABCD_0 \tag{6a}$$

$$\begin{bmatrix} A_t & B_t \\ C_t & D_t \end{bmatrix} = \begin{bmatrix} A_0 & B_0 \\ C_0 & D_0 \end{bmatrix} \begin{bmatrix} 2 & 0 \\ 0 & 1 \end{bmatrix} \begin{bmatrix} A_m & B_m \\ C_m & D_m \end{bmatrix} \begin{bmatrix} A_0 & B_0 \\ C_0 & D_0 \end{bmatrix} \tag{6b}$$

where the ABCD matrix of the lossy transmission line ($ABCD_0$ for the ports and $ABCD_m$ for the impedance transformer) is calculated using [50]:

$$ABCD = \begin{bmatrix} cosh\gamma L & Z\ sinh\gamma \\ (1/Z)\ sinh\gamma L & cosh\gamma L \end{bmatrix} \tag{6c}$$

where $\gamma = \alpha + i\beta$ is the complex propagation constant, L is the length of the CPS transmission line and Z is the complex impedance of the CPS transmission line. We used a 2D simulation to obtain approximate values of Z_0, $Z_m = Z_0/\sqrt{2}$, γ_0 and γ_m of the CPS transmission-line (more details in Appendix A). Then, the scattering parameters were calculated from the ABCD matrix using the following conversion equations [49], [51]:

$$S_{11} = \frac{A_N + (B_N/Z_0) - C_N Z_0 - D_N}{A_N + (B_N/Z_0) + C_N Z_0 + D_N} \tag{7a}$$

$$S_{12} = \frac{2(A_N D_N - B_N C_N)}{A_N + (B_N/Z_0) + C_N Z_0 + D_N} \tag{7b}$$

$$S_{21} = \frac{2}{A_N + (B_N/Z_0) + C_N Z_0 + D_N} \tag{7c}$$

$$S_{22} = \frac{-A_N + (B_N/Z_0) - C_N Z_0 + D_N}{A_0 + (B_N/Z_0) + C_N Z_0 + D_N} \tag{7d}$$

Figure 3 shows the transmission coefficient, S_{21}, and the reflection coefficient, S_{11}, of the TPD calculated from the $ABCD_t$ matrix. It is clear that the series connection of the output ports with impedance transformer $Z_m = Z_0/\sqrt{2}$ introduces very good matching at the design frequency.

In the same manner proposed in [29], [33], switching the matching impedance between $Z_0/\sqrt{2}$ to $\sqrt{2}Z_0$ switches the phase difference between the output ports from 180° out-of-phase to in-phase.

It should be noted that the effect of CPS discontinuities around the impedance transformer has not been included in the Matlab calculation. Moreover, it is not possible to include the ABCD matrices of the three ports simultaneously to estimate the interference between the output ports

(e.g. S_{23}). Furthermore, these calculations do not provide the phase relation between the input and output ports. Consequently, we need to use simulation software to obtain an accurate design and optimum structure.

III. SIMULATIONS

The design was simulated in both time and frequency domains using ANSYS HFSS software. The following material properties are used in the simulations. For Silicon Nitride: $\epsilon_r = 7.6$, $\mu_r = 1$, $\sigma = 0$, and $\tan \delta_e = 0.00526$ [52]. For the gold line: the standard bulk conductivity $\sigma_{au} = 4.1 \times 10^7$ S/m with negligible surface roughness.

A. FREQUENCY DOMAIN SIMULATION

The frequency-domain simulation provides an accurate, deep insight of the design parameters to optimize the geometry of the TPD structure on the thin membrane.

First, HFSS was used to obtain the characteristic impedance and propagation constant of the CPS transmission line used for the input and output ports and $\lambda/4$ impedance transformers. The optimal geometry of the CPS transmission line for the input and output ports minimizes attenuation of the CPS transmission lines for stripline width $W_0 = 45\ \mu$m and separation between striplines $S_0 = 70\ \mu$m [53]. The geometry of the $\lambda/4$ impedance transformer Z_{m1} is $W_1 = 45\ \mu$m, $S_1 = 25\ \mu$m, while the geometry of Z_{m2} is $W_2 = 10\ \mu$m, $S_2 = 70\ \mu$m. More details are presented in Appendix A.

Then, HFSS was used to design the structure of the TPD (shown in Fig. 2(a)) using the CPS-transmission line on a thin membrane. The length of the $\lambda/4$ impedance transformer (which controls the design frequency, f_0) depends on two parameters: the distance between the output ports (Δy) and the angle of the impedance transformer θ. The minimum distance Δy to avoid interference between the waves propagated to the output ports is around 200 μm. This is the main constraint imposed on selecting the design frequency (i.e. the shorter Δy introduces higher f_0). In addition, the angle θ is used to control the design frequency, while also changing the equivalent reactance around the CPS discontinuity which could allow fine-tuning of matching.

Figure 4(a) shows the S-parameters of the optimized TPD structure. As predicted theoretically and shown in Fig. 3, the impedance transformer provides a good matched circuit for all ports around $f_0 = 0.65$ THz. In addition, the transmission coefficient of the output ports is $S_{21} = S_{31} = -3.08$ dB. The -0.08 dB represents the attenuation of the CPS impedance transformer (i.e. -0.6 dB/mm).

Figure 4(b) illustrates the phase relation between the output ports compared to the input port, in addition to the phase shift between the output ports. It's clear that the $\lambda/4$ impedance transformer of impedance $Z_m = Z_0/\sqrt{2}$ introduces a 180° out-of-phase TPD. The electric field of the wave propagated (at $f_0 = 0.65$ THz) through the out-of-phase CPS-TPD structure illustrates that no reflection was observed on the entire structure (as shown in Fig. 6(c)).
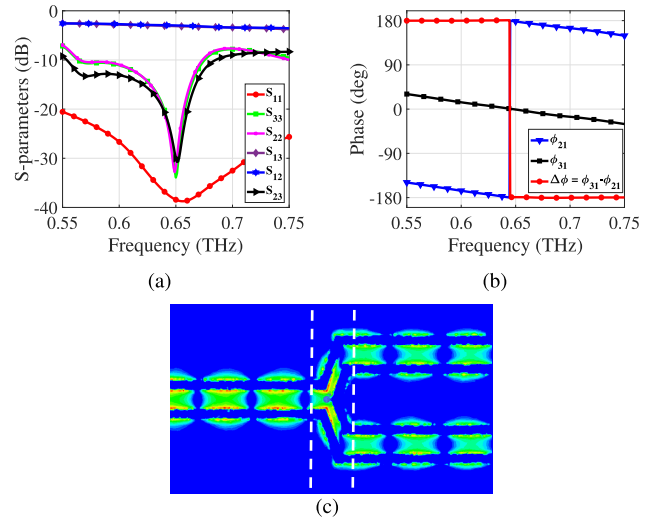

FIGURE 4. (a) S-parameters of the 180° out-of-phase CPS-TPD. (b) Phase relation between ports. (c) Electric field propagation through the CPS-TPD at $f_0 = 0.65$ THz.
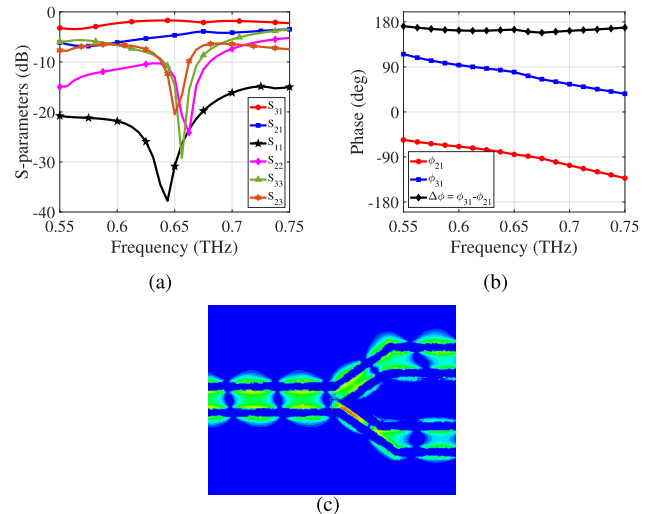

FIGURE 5. (a) S-parameters of the 180° out-of-phase CPS-TPD with power division ratio $\alpha = 2$. (b) Phase relation between ports. (c) Electric field propagation through the CPS-TPD.

To demonstrate the ability to control the power division between the output ports, we used equations (2) and (3) to design a power divider with power division ratio $\alpha = 2$ (i.e. $P_3 = 2P_2$). By substituting in these equations, the equivalent input impedance of the two ports will be $Z_{2i} = Z_1/3$ and Z_{3i} z $2Z_1/3$. Therefore, the $\lambda/4$ impedance transformer must have $Z_{m\alpha2} = Z_1/\sqrt{3}$ and $Z_{m\alpha3} = \sqrt{2/3}Z_1$ with a CPS-geometry of $W_{m\alpha2} = 45\ \mu$m, $S_{m\alpha2} = 10\ \mu$m and $W_{m\alpha3} = 45\ \mu$m, $S_{m\alpha3}$ z 38 μm, respectively (the impedances $Z_{m\alpha2}$ and $Z_{m\alpha3}$ presented in appendix A). Figure 5(a) shows that input power is divided by a division ratio $\alpha = 2$ for which the transmission coefficients of the output ports are $S_{21} = -4.8$ dB and $S_{31} = -1.8$ dB with a 180° phase difference as shown in Fig. 5(b). Figure 5(c) shows that the intensity of the electric field of the propagated wave at the output port 3 is higher than of the output port 2.
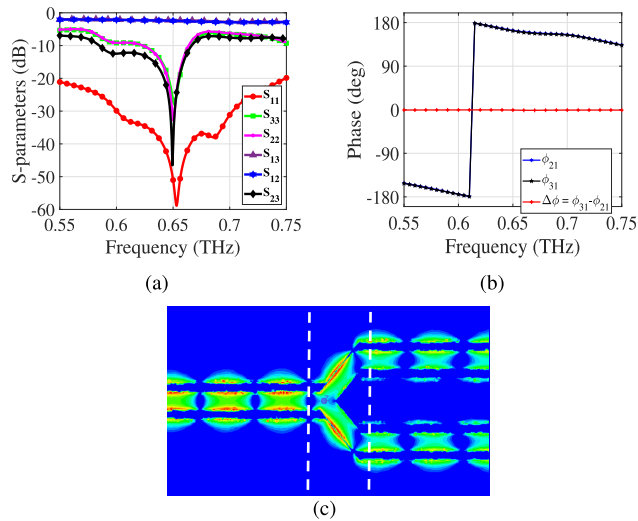
FIGURE 6. (a) S-parameters of the in-phase TPD. (b) Phase relation between ports. (c) Electric field propagation through the in-phase TPD at $f_0 = 0.65$ THz.
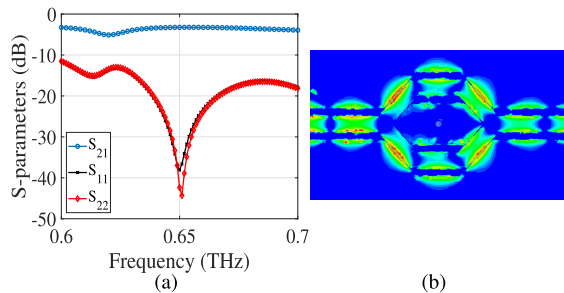

FIGURE 7. (a) S-parameters of the combiner structure. (b) The electric field propagation through the combiner structure.

Next, we explored the in-phase TPD using the CPS transmission line. Figure 6 shows the simulation results of the in-phase TPD. We explored using a matching impedance of $Z_{m2} = \sqrt{2}Z_0$ with a CPS geometry of $W_2 = 10$ μm, $S_2 = 70$ μm, which introduces better matching at the design frequency $f_0 = 0.65$ THz. On the other hand, it reduces the output waves, S_{21} and S_{31}, to -3.1 dB due to the higher attenuation of the CPS (i.e. -1 dB/mm).

To investigate the operation of the in-phase TPD structure as a THz wave combiner, we simulated a structure that consists of two mirrored in-phase TPDs; the first part is used to divide the input wave into two identical in-phase waves while the second one is used to combine these waves. Figure 7 shows the calculated S-parameters illustrating that the reflection at the input port, S_{11}, at the design frequency ($f_0 = 0.65$ THz) is minimum, emphasizing a good matching for both TPD and THz combiner structures.

B. TIME DOMAIN SIMULATION
The time-domain simulation characterizes the excitation of the structure and analyzes the spectrum of transmitted and received pulses. We used the optimized structure of the in-phase TPD obtained by the frequency-domain solver.
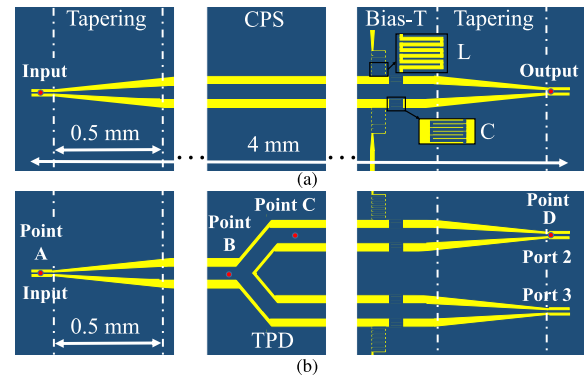

FIGURE 8. The Schematic diagram of (a) the reference structure. (b) the TPD structure using CPS transmission-line on a thin-membrane.
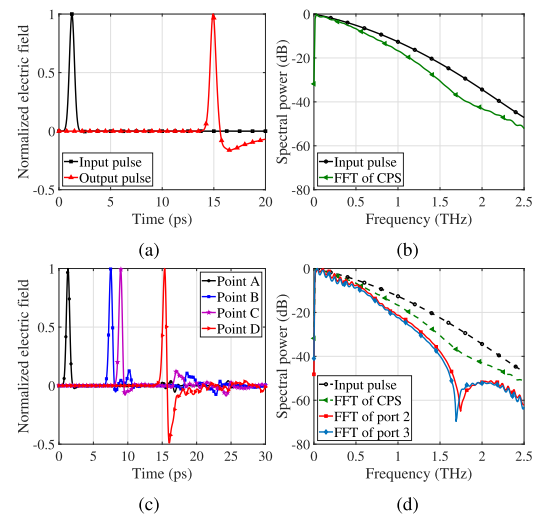

FIGURE 9. Time domain simulation results: (a) Input and output pulses of the reference structure. (b) Spectral power density of the input and output pulses. (c) Pulse after propagation through the TPD structure at different points. (d) Spectral power density of input and output pulses of the TPD.

The dimensions of the 0.4 μm-thick LTG-GaAs chips (introduced in [1]) used for the transmitter and receiver are 20 μm $\times$ 40 μm. Two 12.5 μm $\times$ 10 μm gold contact pads, separated by a 5 μm gap, are patterned on these chips using photolithography to form each PCS. These dimensions are chosen as a compromise between ease of handling and contacting, which favor larger contacts, and minimizing radiation, which favors smaller. These PCS dimensions constrain the geometry of the CPS at input and output ports to be $W_{in} = S_{in} = 10$ μm. These small PCS dimensions, and the resulting narrow CPS geometry, minimize radiation at higher frequencies during excitation since S_{in} z $2W_{in} \ll \lambda_0/2$ at, for example, 3 GHz, forming an inefficient dipole radiator. We then tapered the narrow CPS to a wider CPS ($W_0 = 45$ μm, $S_0 = 70$ μm) to minimize the attenuation of the transmission line. More details were described in [53]. The optimal tapering length which introduces an acceptable reflection is 0.5 mm. Furthermore, a Bias-T configuration which consists of a meander inductor and an interdigitated capacitor was designed to connect the bias voltage to the transmitting PCS (through the inductor) and block the bias
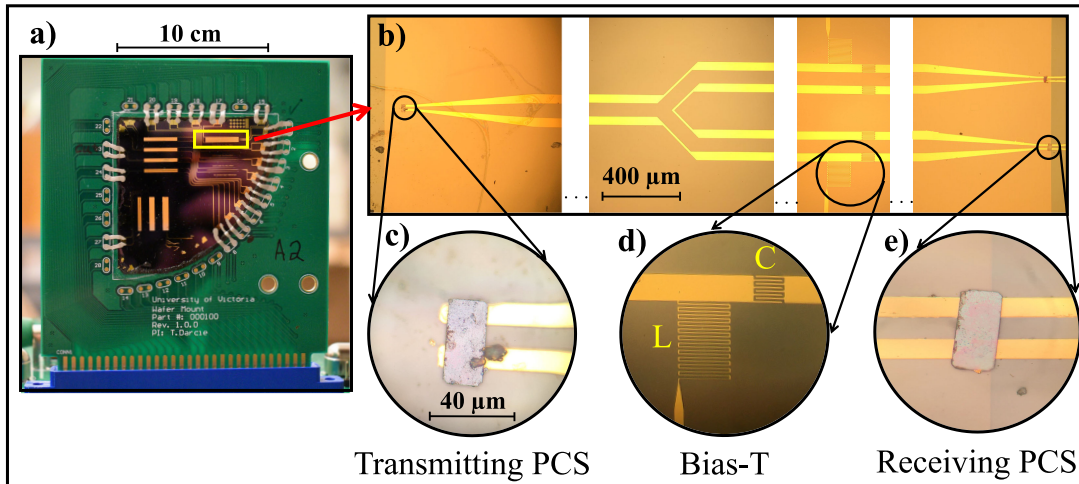
FIGURE 10. (a) The fabricated membrane-based TSoCs mounted on a printed circuit board (PCB). (b) Microscope image of CPS-TPD structure. (c) Microscope image of transmitting PCS (gold contacts are face down to contact gold lines). (d) Microscope image of the Bias-T configuration. (e) Microscope image of the receiving PCS.

from the receiving PCSs (by the interdigitated capacitor). These structures were designed separately to enhance the efficiency of the TSoC.

To investigate the amplitude response of the TPD, we compared the received pulses of two structures; the first is the reference structure (i.e. tapering, CPS, and Bias-T without the TPD), and the second structure that includes the tapering, Bias-T, CPS and the TPD (as shown in Fig. 8). The length of the simulated structures is 4 mm while the fabricated structure is 10 mm (for computational efficiency). We excite these structures with a Gaussian pulse, with full width at half maximum (FWHM) = 1 ps, similar to the pulse generated from the active PCS, calculate the electric field of the pulse after propagation through the two structures and then calculate the spectral power density of these pulses.

Figure 9(a) illustrates the normalized electric field of the input and output pulses of the reference structure while the spectral response of the output pulse is shown in Fig. 9(b). Figure 9(c) shows the normalized electric field of the pulse propagated through the TPD structure at different points (i.e. A, B, C and D) to investigate the effect of different structures on the pulse-shape. The pulses at the points B and C, respectively, are considered as the input and output pulses of the TPD structure, while the pulse at point D is the estimated output pulse of the entire TSoC. It should be noted that the $\lambda/4$ impedance transformer provides good matching at a certain frequency, f_0, and the mismatch at the other frequencies produces a spectral reflections, these reflections appeared in the pulses at points C and D and produce a power imbalance between the output ports. This power imbalance is shown in Fig. 9(d) which illustrates the spectral response of the received pulses of the TPD structure.

IV. EXPERIMENTAL MEASUREMENTS

Figure 10 shows the fabricated CPS-TPD, as one of many circuits, on a 1 μm-thin Si_3N_4 membrane. A series of procedures

were processed to fabricate the membrane-based TSoC; a 1 μm-thin layer of Si_3N_4 was deposited on a quarter of a 500 μm-thick double-sided polished (DSP) Si wafer. Next, we used photolithography to define the membrane windows (on the lower side of the Si wafer) and etch these areas using Potassium Hydroxide (KOH). Then, photolithography was used to define the metallic structures on the upper-side of the wafer. After that, physical vapour deposition (PVD) was used to deposit a 15 nm layer of Titanium (Ti) as an adhesion layer between the membrane and a 200 nm layer of gold (Au). Finally, the thin LTG-GaAs PCSs were bonded to the CPS (at the positions of the input and output ports) using a drop of deionized (DI) water to create a Van der Waals (VDW) bond.

The THz time-domain spectroscopy (TDS) measurement setup shown in Fig.11 was used to generate and detect THz pulses [54]. The transmitting PCS was biased through the inductor of the Bias-T with 25V DC voltage. A 90 fs laser pulse (wavelength = 780 nm, repetition rate = 80 MHz) was divided by a beam splitter into two paths; one is directed to excite the transmitting PCS through an optical chopper; the other goes through a mechanical optical delay line (sweeping velocity = 0.02 mm/s) and is then focused on the receiving PCS. The receiving PCS is similar to the transmitter but without DC bias which was blocked using the interdigitated capacitor of the Bias-T. The optical chopper in the transmitter path modulates the laser pulse train at a known frequency (e.g. 1.1 kHz). The reference signal of the chopper is connected to a lock-in amplifier. The received pulse is plotted by sweeping the physical path-length difference between transmitter and receiver using the repetitive photoconductive sampling method [54]–[56].

It should be noted that the experimental setup enables the measurement at one of the output ports. So, the same installation setup (i.e. the same bias voltage, the same current of the laser source and the same alignment of the laser beam
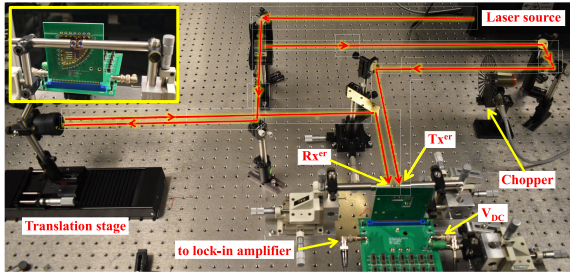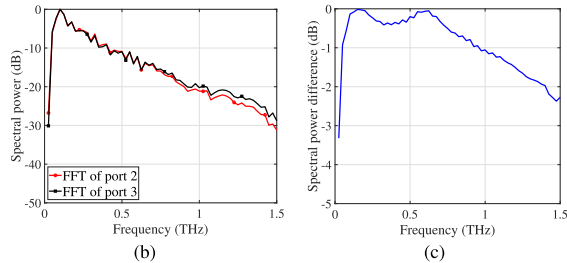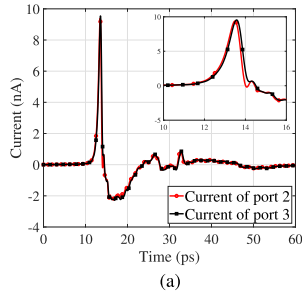
FIGURE 11. TDS measurement setup.

FIGURE 12. Experimental measurements: (a) The measured current of the output ports. (b) The spectral power density of the measured current. (c) The difference between the spectral power density of the measured output pulses.

on both output ports) was assured for the measurement of both output ports.

Figure 12(a) illustrates the measured current pulses at the output ports, with peak currents of 9.35 nA and 9.5 nA. The measured pulses show close agreement with the simulation (shown in Fig. 9(c)). The zoomed-in inset on Fig. 12(a) shows a time-shift of 0.08 ps between the measured pulses at the two receivers, which corresponds to an approximate 20 μm placement-inaccuracy of the receiver PCSs. Figure 12(b) shows the spectral power density of received pulses obtained by applying the Fast Fourier Transform (FFT) to the measured pulse. One well-known challenge of this type of THz system experiment is the lack of a direct measurement probe to measure an absolute amplitude (or attenuation) at different points of the structure (e.g. before and after the TPD). Therefore, to compare the spectral response of the measured-pulses, we normalized the spectral response of the measured pulses to the maximum value such that the maximum was 0 dB. Also, we noticed an increase in the spectral power density around the 1.3 THz. This increase could be caused by the Fabry–Pérot resonance due to the $\lambda/4$ impedance transformers. The resonant frequency, f_f, for a cavity with length l and refractive index of the substrate n is calculated by $f_f = c/2nl$ leading
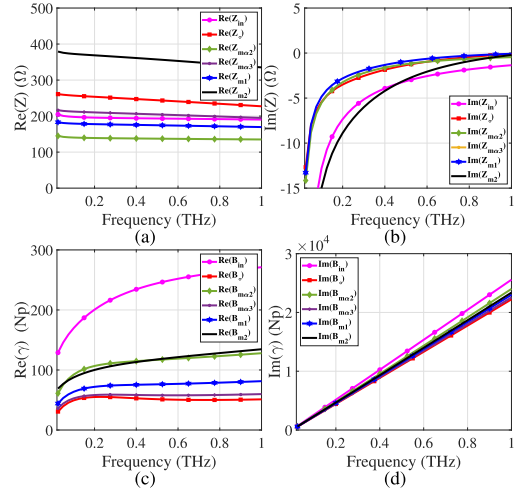

FIGURE 13. Frequency-domain simulation results of different CPS geometries. (a) Re(Z). (b) Im(Z). (c) Re(γ) = α. (d) Im(γ) = β.

to a resonant frequency of the $\lambda/4$ impedance transformer of $f_f = c/2n(\lambda_n/4) = 2f_0 = 1.3$ THz. The difference between the spectral power density of both pulses is negligible at the design frequency of 0.65 THz (due to the good-matching at this frequency) and less than 1 dB power imbalance over a wide spectrum up to 1 THz as shown in Fig. 12(c).

V. CONCLUSION

In this paper, we introduced the theory and simulation results of THz power dividers, either 180° out-of-phase or in-phase, using a $\lambda/4$ impedance transformer with line impedances of $Z_0/\sqrt{2}$ and $\sqrt{2}Z_0$ respectively. The operation of the in-phase TPD as a THz wave combiner was investigated using ANSYS HFSS due to the difficulty of experimental validation. We demonstrated experimentally an in-phase TPD using the CPS transmission-line on a 1 μm-thin Si_3N_4 membrane. The peak currents of the measured pulses are around 9.5 nA, the spectral power density of the received pulses are identical at the design frequency of 0.65 THz and a minor power-imbalance (less than 1 dB) was achieved over a wide spectrum up to 1 THz.

This attractive THz platform enables potential future applications such as terabit millimeter-wave circuits, imaging systems and compact/efficient waveguide-based THz spectroscopy systems. The TPD will be a key element in future applications where we plan to perform coherent measurements on a selection of devices under test.

APPENDIX A - THE SIMULATION RESULTS OF THE CPS TRANSMISSION-LINE
ANSYS HFSS was used to obtain the complex impedances and propagation constants of the CPS transmission lines of different geometry (i.e. the ports and the $\lambda/4$ impedance transformer) as shown in Fig. 13.

ACKNOWLEDGEMENT

REFERENCES

[1] R. Smith and T. Darcie, "Demonstration of a low-distortion tera-hertz system-on-chip using a CPS waveguide on a thin membrane substrate," *Opt. Exp.*, vol. 27, no. 10, p. 13653, May 2019, doi: 10.1364/OE.27.013653.

[2] J. Hirokawa, K. Sakurai, M. Ando, and N. Goto, "An analysis of a waveguide t junction with an inductive post," *IEEE Trans. Microw. Theory Techn.*, vol. 39, no. 3, pp. 563–566, Mar. 1991, doi: 10.1109/22.75301.

[3] H.-W. Yao, A. E. Abdelmonem, J.-F. Liang, X.-P. Liang, K. A. Zaki, and A. Martin, "Wide-band waveguide and ridge waveguide T-junctions for diplexer applications," *IEEE Trans. Microw. Theory Techn.*, vol. 41, no. 12, pp. 2166–2173, Dec. 1993, doi: 10.1109/22.260702.

[4] G.-L. Huang, S.-G. Zhou, T.-H. Chio, and T.-S. Yeo, "Design of a symmetric rectangular waveguide T-junction with in-phase and unequal power split characteristics," in *Proc. IEEE Antennas Propag. Soc. Int. Symp. (APSURSI)*, Orlando, FL, USA, Jul. 2013, pp. 2119–2120, doi: 10.1109/APS.2013.6711718.

[5] S. W. Wong and L. Zhu, "Ultra-wideband power divider with good in-band splitting and isolation performances," *IEEE Microw. Wireless Compon. Lett.*, vol. 18, no. 8, pp. 518–520, Aug. 2008, doi: 10.1109/LMWC.2008.2001009.

[6] C.-M. Lin, H.-H. Su, J.-C. Chiu, and Y.-H. Wang, "Wilkinson power divider using microstrip EBG cells for the suppression of harmonics," *IEEE Microw. Wireless Compon. Lett.*, vol. 17, no. 10, pp. 700–702, Oct. 2007, doi: 10.1109/LMWC.2007.905595.

[7] J.-P. Wang, J. Ni, Y.-X. Guo, and D.-G. Fang, "Miniaturized microstrip wilkinson power divider with harmonic suppression," in *Proc. IEEE MTT-S Int. Microw. Workshop Ser. Art Miniaturizing RF Microw. Passive Compon.*, Chengdu, China, Dec. 2008, pp. 227–229, doi: 10.1109/IMWS.2008.4782307.

[8] R. Mirzavand, M. M. Honari, A. Abdipour, and G. Moradi, "Compact microstrip wilkinson power dividers with harmonic suppression and arbitrary power division ratios," *IEEE Trans. Microw. Theory Techn.*, vol. 61, no. 1, pp. 61–68, Jan. 2013, doi: 10.1109/TMTT.2012.2226054.

[9] J. He, W. Luo, and S. Chen, "A gysel power divider with enhanced isolation bandwidth," in *Proc. Asia–Pacific Microw. Conf. (APMC)*, Nanjing, China, Dec. 2015, pp. 1–3, doi: 10.1109/APMC.2015.7413356.

[10] J. Papapolymerou, G. E. Ponchak, and E. M. Tentzeris, "A wilkinson power divider on a low resistivity Si substrate with a polyimide interface layer for wireless circuits," in *IEEE MTT-S Int. Microw. Symp. Dig.*, Seattle, WA, USA, vol. 1, Jun. 2002, pp. 593–596, doi: 10.1109/MWSYM.2002.1011690.

[11] Y. Zhichao, L. Shanshan, B. Feng, Z. Mingmin, Z. Peng, and W. Wenfeng, "A novel wideband balun with a CPW power divider," in *Proc. Asia–Pacific Int. Symp. Electromagn. Compat. (APEMC)*, Shenzhen, China, May 2016, pp. 652–655, doi: 10.1109/APEMC.2016.7522826.

[12] K. Al Shamaileh, N. Dib, and S. Abushamleh, "A compact coplanar waveguide wilkinson power divider based on signal traces and adjacent grounds width modulation," *Microw. Opt. Technol. Lett.*, vol. 60, no. 9, pp. 2224–2227, Sep. 2018, doi: 10.1002/mop.31332.

[13] H. Jaradat, N. Dib, and K. Al Shamaileh, "Miniaturized dual-band CPW wilkinson power divider using T-network adopting series stubs with a high frequency ratio," *AEU-Int. J. Electron. Commun.*, vol. 107, pp. 32–38, Jul. 2019.

[14] M. Zou, Z. Yin, Z. Shao, L. Liu, and X. Zhu, "Design of ka-band substrate integrated waveguide power dividers/combiners," in *Proc. Int. Conf. Comput. Problem-Solving (ICCP)*, Oct. 2011, pp. 361–363, doi: 10.1109/iccps.2011.6092240.

[15] A. P. Wirawan, P. H. Mukti, and E. Setijadi, "Design of sub-strate integrated waveguide based power divider for S-band applications," in *Proc. Int. Conf. Radar, Antenna, Microw., Electron. Telecommun. (ICRAMET)*, Bandung, Indonesia, Oct. 2015, pp. 28–31, doi: 10.1109/ICRAMET.2015.7380768.

[16] S. Germain, D. Deslandes, and K. Wu, "Development of substrate integrated waveguide power dividers," in *Proc. Can. Conf. Electr. Comput. Eng. Toward Caring Humane Technol. (CCECE)*, Montreal, QC, Canada, vol. 3, 2003, pp. 1921–1924, doi: 10.1109/CCECE.2003.1226289.

[17] K. Chen, B. Yan, and R. Xu, "A novel W-band ultra-wideband sub-strate integrated waveguide (SIW) T-junction power divider," in *Proc. Int. Symp. Signals, Syst. Electron.*, Nanjing, China, 2010, pp. 1–3, doi: 10.1109/ISSSE.2010.5638214.

[18] X. Zou, C.-M. Tong, and D.-W. Yu, "Y-junction power divider based on substrate integrated waveguide," *Electron. Lett.*, vol. 47, no. 25, pp. 1375–1376, Dec. 2011, doi: 10.1049/el.2011.2953.

[19] G. Siso, J. Bonache, and F. Martin, "Dual-band Y-junction power dividers implemented through artificial lines based on complementary resonators," in *IEEE MTT-S Int. Microw. Symp. Dig.*, Atlanta, GA, USA, Jun. 2008, pp. 663–666, doi: 10.1109/MWSYM.2008.4632919.

[20] A. M. Abbosh, M. E. Bialkowski, and J. Mazierska, "An UWB planar out-of-phase power divider employing microstrip-slot and parallel stripline-microstrip transitions," in *Proc. Asia–Pacific Microw. Conf.*, Yokohama, Japan, Dec. 2006, pp. 905–908, doi: 10.1109/APMC.2006.4429559.

[21] B. Xiao, H. Yao, M. Li, J.-S. Hong, and K. L. Yeung, "Flexible wide-band microstrip-slotline-microstrip power divider and its application to antenna array," *IEEE Access*, vol. 7, pp. 143973–143979, 2019, doi: 10.1109/ACCESS.2019.2944462.

[22] M. E. Bialkowski and A. M. Abbosh, "Design of a compact uwb out-of-phase power divider," *IEEE Microw. Wireless Compon. Lett.*, vol. 17, no. 4, pp. 289–291, Apr. 2007, doi: 10.1109/LMWC.2007.892979.

[23] F. Lin, Q.-X. Chu, Z. Gong, and Z. Lin, "Compact broadband gysel power divider with arbitrary power-dividing ratio using microstrip/slotline phase inverter," *IEEE Trans. Microw. Theory Techn.*, vol. 60, no. 5, pp. 1226–1234, May 2012, doi: 10.1109/TMTT.2012.2187067.

[24] K. Song and Q. Xue, "Novel ultra-wideband (UWB) multilayer slot-line power divider with bandpass response," *IEEE Microw. Wireless Compon. Lett.*, vol. 20, no. 1, pp. 13–15, Jan. 2010, doi: 10.1109/LMWC.2009.2035951.

[25] L. Xiao, H. Peng, T. Yang, and J. Dong, "Power divider based on stepped-impedance slotline," *Prog. Electromagn. Res. C*, vol. 50, pp. 147–154, Jan. 2014, doi: 10.2528/PIERC14042903.

[26] M. Leib, A. Vollmer, and W. Menzel, "In-phase and anti-phase power dividers for UWB differentially fed antenna arrays," *IEEE Antennas Wireless Propag. Lett.*, vol. 9, pp. 455–458, 2010, doi: 10.1109/LAWP.2010.2050571.

[27] P. Wu, Y. Zhang, Y.-L. Dong, and Q. Zhang, "A novel Ka-band pla-nar balun using microstrip-CPS-microstrip transition," *IEEE Microw. Wireless Compon. Lett.*, vol. 21, no. 3, pp. 136–138, Mar. 2011, doi: 10.1109/LMWC.2010.2104315.

[28] M.-Z. Wang, F.-S. Zhang, J. Sun, K. Chen, and B. Wen, "Design of several power dividers using CPW-to-microstrip transition," *Prog. Electromagn. Res. Lett.*, vol. 41, pp. 125–134, Jan. 2013, doi: 10.2528/PIERL13060306.

[29] L. Fan and K. Chang, "Uniplanar power dividers using coupled CPW and asymmetrical CPS for MICs and MMICs," *IEEE Trans. Microw. Theory Techn.*, vol. 44, no. 12, pp. 2411–2420, Dec. 1996, doi: 10.1109/22.554570.

[30] T. Laneve, K. Hettak, C. J. Verver, P. Beland, and M. G. Stubbs, "A novel reduced-size uniplanar wilkinson power divider using ACPS series stubs," in *Proc. 30th Eur. Microw. Conf.*, Paris, France, Oct. 2000, pp. 1–4, doi: 10.1109/EUMA.2000.338873.

[31] M. C. Scardelletti, G. E. Ponchak, and T. M. Weller, "Miniaturized wilkinson power dividers utilizing capacitive loading," *IEEE Microw. Wireless Compon. Lett.*, vol. 12, no. 1, pp. 6–8, Jan. 2002, doi: 10.1109/7260.975717.

[32] K. Hettak, G. A. Morin, and M. G. Stubbs, "Compact MMIC CPW and asymmetric CPS branch-line couplers and wilkinson dividers using shunt and series stub loading," *IEEE Trans. Microw. Theory Techn.*, vol. 53, no. 5, pp. 1624–1635, May 2005, doi: 10.1109/TMTT.2005.847052.

[33] L. Fan and K. Chang, "A 180° out-of-phase power divider using asymmet-rical coplanar stripline," *IEEE Microw. Guided Wave Lett.*, vol. 6, no. 11, pp. 404–406, Nov. 1996, doi: 10.1109/75.541454.

[34] K. W. Wong, L. Chiu, and Q. Xue, "Uniplanar power dividers using asymmetric coplanar striplines and slotlines," in *Proc. 38th Eur. Microw. Conf.*, Amsterdam, The Netherlands, Oct. 2008, pp. 337–340, doi: 10.1109/EUMC.2008.4751457.

[35] K. S. Reichel, R. Mendis, and D. M. Mittleman, "A broadband terahertz waveguide T-junction variable power splitter," *Sci. Rep.*, vol. 6, no. 1, Sep. 2016, Art. no. 28925, doi: 10.1038/srep28925.

[36] Z. Niu, B. Zhang, Y. Fan, and X. Chen, "The design of 220 GHz waveguide power divider for multi-channel radiometer front end," in *Proc. 10th UK-Eur.-China Workshop Millimetre Waves THz Technol. (UCMMT)*, Liverpool, U.K., Sep. 2017, pp. 1–3, doi: 10.1109/UCMMT.2017.8068498.

[37] H. Zhang, D. Y. Shao, and Y. Shao, "A broadband millimeter-wave waveguide power divider with high isolation," *Amer. J. Phys. Appl.*, vol. 7, no. 4, pp. 101–108, Jul. 2019, doi: 10.11648/j.ajpa.20190704.12.

[38] S. Horst, R. Bairavasubramanian, M. M. Tentzeris, and J. Papapolymerou, "Modified wilkinson power dividers for millimeter-wave integrated circuits," *IEEE Trans. Microw. Theory Techn.*, vol. 55, no. 11, pp. 2439–2446, Nov. 2007, doi: 10.1109/TMTT.2007.908672.

[39] E. A. Abbas and A. M. Abbosh, "Tunable millimeter-wave power divider for future 5G cellular networks," in *Proc. IEEE Int. Symp. Antennas Propag. (APSURSI)*, Fajardo, Puerto Rico, Jun. 2016, pp. 1715–1716, doi: 10.1109/APS.2016.7696564.

[40] A. Treizebre, S. Laurette, Y. Xu, R. G. Bosisio, and B. Bocquet, "THZ power divider circuits on planar Goubau lines (PGLS)," *Prog. Electromagn. Res. C*, vol. 26, pp. 219–228, Jan. 2012, doi: 10.2528/PIERC11112409.

[41] Y. Li, J.-R. Hu, and J.-S. Li, "Tunable terahertz power divider based on graphene plasmonic waveguide," *Proc. SPIE*, vol. 10030, pp. 441–446, Nov. 2016, doi: 10.1117/12.2247131.

[42] Y. Liu, Y. Yuan, X. Lv, and L.-M. Si, "Design of 0.5 THz 2D square lattice EBG waveguide transmission line and power-divider using MEMS technology," *Proc. SPIE*, vol. 7385, pp. 497–504, Aug. 2009, doi: 10.1117/12.835616.

[43] K. Xiaoke, C. Peng, D. Xianjin, C. Zhang, J. Jun, M. Li, and C. Binbin, "Design method about 0.14 THz power divider based on 3 dB directional coupler," *Hongwai yu Jiguang Gongcheng/Infrared Laser Eng.*, vol. 43, pp. 2907–2911, Sep. 2014.

[44] Y. Zhang, J. Yin, and H. Wang, "Millimeter-wave broadband power divider using substrate integrated coaxial line," in *Proc. 11th UK-Eur.-China Workshop Millim. Waves THz Technol. (UCMMT)*, HangZhou, China, Sep. 2018, pp. 1–4, doi: 10.1109/UCMMT45316.2018.9015671.

[45] C. Li, L. B. Lok, A. Khalid, V. Papageorgiou, J. Grant, and D. R. S. Cumming, "Millimeter-wave coplanar stripline power dividers," *Int. J. Microw. Wireless Technol.*, vol. 5, no. 3, pp. 205–212, Jun. 2013, doi: 10.1017/S1759078713000421.

[46] P. Daud, D. P. Kurniadi, D. Mahmudin, Y. N. Wijayanto, P. Putranto, E. J. Pristianto, A. Nurrahman, Andriana, Zulkarnaen, and O. Vertus, "10 GHz optical modulator using CPS structure for communication and sensing," *IOP Conf. Ser., Mater. Sci. Eng.*, vol. 622, Nov. 2019, Art. no. 012018, doi: 10.1088/1757-899x/622/1/012018.

[47] H.-K. Chiou, H.-H. Lin, and C.-Y. Chang, "Balun design for uniplanar broad band double balanced mixer," *Electron. Lett.*, vol. 31, no. 24, pp. 2113–2114, Nov. 1995, doi: 10.1049/el:19951404.

[48] K. Tilley, K. Chang, and X.-D. Wu, "Coplanar waveguide fed coplanar strip dipole antenna," *Electron. Lett.*, vol. 30, no. 3, pp. 176–177, Feb. 1994, doi: 10.1049/el:19940181.

[49] D. Pozar, *Microwave Engineering*, 4th ed. Hoboken, NJ, USA: Wiley, 2005.

[50] C. R. Paul, *Analysis of Multiconductor Transmission Lines*, 2nd ed. Hoboken, NJ, USA: Wiley, 2007.

[51] D. A. Frickey, "Conversions between S, Z, Y, H, ABCD, and T parameters which are valid for complex source and load impedances," *IEEE Trans. Microw. Theory Techn.*, vol. 42, no. 2, pp. 205–211, Feb. 1994, doi: 10.1109/22.275248.

[52] G. Cataldo, J. A. Beall, H.-M. Cho, B. McAndrew, M. D. Niemack, and E. J. Wollack, "Infrared dielectric properties of low-stress silicon nitride," *Opt. Lett.*, vol. 37, no. 20, p. 4200, Oct. 2012, doi: 10.1364/OL.37.004200.

[53] W. Gomaa, L. Smith, V. Shiran, and T. Darcie, "Terahertz low-pass filter based on cascaded resonators formed by CPS bending on a thin membrane," *Opt. Exp.*, vol. 28, no. 21, pp. 31967–31978, 2020, Oct. 2020, doi: 10.1364/OE.403702.

[54] Y. S. Lee, *Principles of Terahertz Science and Technology*. New York, NY, USA: Springer, 2009. [Online]. Available: https://link.springer.com/book/10.1007/978-0-387-09540-0

[55] M. C. Nuss and J. Orenstein, "Terahertz time-domain spectroscopy," in *Millimeter and Submillimeter Wave Spectroscopy of Solids* (Topics in Applied Physics), vol. 74, G. Grüner, Eds. Berlin, Germany: Springer, 1998, ch. 2, pp. 7–50, doi: 10.1007/BFb0103419.

[56] E. Castro-Camus, L. Fu, J. Lloyd-Hughes, H. H. Tan, C. Jagadish, and M. B. Johnston, "Photoconductive response correction for detectors of terahertz radiation," *J. Appl. Phys.*, vol. 104, no. 5, Sep. 2008, Art. no. 053113, doi: 10.1063/1.2969035.

WALID GOMAA was born in Giza, Egypt, in 1985. He received the B.Sc. degree in electrical engineering and the M.Sc. degree in engineering physics from the Military Technical College (MTC), Cairo, Egypt, in 2007 and 2015 respectively. He is currently pursuing the Ph.D. degree in electrical and computer engineering with the University of Victoria, BC, Canada, under the supervision of Professor Thomas Darcie. His research interests include design and fabrication of the THz system-on-chip, THz wave-guided systems, laser imaging, and spectroscopy.

ROBERT LEVI SMITH (Member, IEEE) was born in Richmond, BC, Canada, in 1988. He received a technologist diploma from the Okanagan College, Canada, in 2008, the B.Eng. degree in electrical engineering from the University of Victoria (UVic), Canada, in 2011, and the M.A.Sc. and Ph.D. degrees from UVic, in 2014 and 2019, respectively, under the supervision of Professor Thomas Darcie. He is currently a Postdoctoral Researcher with Prof. Darcie's group. His primary research interest is focused on advancing terahertz devices and systems towards industry.

HADI ESMAEILSABZALI received the Ph.D. degree in mechatronic systems engineering from Simon Fraser University (SFU), in 2017. He is currently working as a Process Engineer with the 4D LABS, SFU. His research interests include (Bio) MEMS, liquid biopsy, and point-of-care testing devices.

THOMAS E. DARCIE (TED) (Fellow, IEEE) received the Ph.D. degree in aerospace from the University of Toronto, in 1982.

He then joined AT&T Bell Laboratories, Crawford Hill, NJ, to study lightwave telecommunications, including fiber fabrication processes, semiconductor lasers, optical amplifiers, and numerous modulation and multiplexing techniques. He has been a lead figure in the development of lightwave networks for broadband access, cable television, and wireless communications. As head of access communications research at AT&T Bell Labs, from 1989 to 1995, he was responsible for technology innovation in wireless, optical access,s and hybrid fiber-coax systems. As AT&T Labs Vice President and the Director of the Communications Infrastructure Research Lab, from 1995 to 2002, he led a research laboratory that provided technology support for AT&T's diverse requirements in optical networking, broadband access, fixed wireless access, wireless local-area networks, and cellular systems. As a Professor and Tier 1 Canada Research Chair, from 2003 to 2020, at the University of Victoria, his research focused on systems for communications, broadband and real-time networks, optical imaging, microwave and terahertz photonics. He is an AT&T Fellow, a Fellow of the Optical Society of America, a Fellow of the Canadian Academy of Engineering, an alumnus of the National Academy of Engineering – CSTB, and collaborated with Microsoft Research as a Visiting Scientist, from 2015 to 2018. As a founding Director of Engineering Entrepreneurship at UVic, he co-founded and advises several companies. He led in the creation of UVic's Masters of Engineering in applied data science and Matrix Institute for applied data science which he co-directs.

• • •